molecules

MDPI

Article

Theoretical Analysis of Superior Photodegradation of Methylene Blue by Cerium Oxide/Reduced Graphene Oxide vs. Graphene

Nguyen Hoang Hao [1], Phung Thi Lan [2], Nguyen Ngoc Ha [2], Le Minh Cam [2,3] and Nguyen Thi Thu Ha [2,*]

[1] College of Education, Vinh University, 182 Le Duan, Vinh 460000, Vietnam; haonguyen0404@gmail.com
[2] Faculty of Chemistry, Hanoi National University of Education, 136 Xuan Thuy, Cau Giay, Hanoi 100000, Vietnam; lanpt@hnue.edu.vn (P.T.L.); hann@hnue.edu.vn (N.N.H.); camlm@hnue.edu.vn (L.M.C.)
[3] Faculty of Pharmacy, Thanh Do University, QL32, Kim Chung, Hoai Duc, Hanoi 100000, Vietnam
* Correspondence: ntt.ha@hnue.edu.vn

Abstract: Density functional theory and a semi-empirical quantum chemical approach were used to evaluate the photocatalytic efficiency of ceria (CeO_2) combined with reduced graphene oxide (rGO) and graphene (GP) for degrading methylene blue (MB). Two main aspects were examined: the adsorption ability of rGO and GP for MB, and the separation of photogenerated electrons and holes in CeO_2/rGO and CeO_2/GP. Our results, based on calculations of the adsorption energy, population analysis, bond strength index, and reduced density gradient, show favorable energetics for MB adsorption on both rGO and GP surfaces. The process is driven by weak, non-covalent interactions, with rGO showing better MB adsorption. A detailed analysis involving parameters like fractional occupation density, the centroid distance between molecular orbitals, and the Lewis acid index of the catalysts highlights the effective charge separation in CeO_2/rGO compared to CeO_2/GP. These findings are crucial for understanding photocatalytic degradation mechanisms of organic dyes and developing efficient photocatalysts.

Keywords: CeO_2; rGO; graphene; DFT+U; methylene blue; GFN-xTB

Citation: Hao, N.H.; Lan, P.T.; Ha, N.N.; Cam, L.M.; Ha, N.T.T. Theoretical Analysis of Superior Photodegradation of Methylene Blue by Cerium Oxide/Reduced Graphene Oxide vs. Graphene. *Molecules* **2024**, *29*, 3821. https://doi.org/10.3390/molecules29163821

Academic Editors: Aleksander Czekanski and Cuiying Jian

Received: 14 July 2024
Revised: 5 August 2024
Accepted: 8 August 2024
Published: 12 August 2024

1. Introduction

Dye pollutants stand out as persistent and problematic contaminants in water bodies within the context of environmental issues [1]. Photocatalysis, which uses catalysts and light to degrade dyes into harmless compounds, offers a promising solution for sustainable dye treatment and has emerged as an effective method for addressing this problem [2].

Among the variety of photocatalytic materials, ceria (cerium oxide, CeO_2) is considered one of the most promising for dye treatment due to its high efficiency, non-toxicity, photochemical stability, affordability, and its excellent ability to switch between Ce^{3+} and Ce^{4+} states, thereby enhancing catalytic efficiency in various reactions. However, ceria catalysts also exhibit limitations that hinder their practical applications. One significant drawback is their typically small specific surface area, which can limit photocatalytic efficiency. More critically, ceria suffers from a high rate of electron–hole recombination, a major challenge in photocatalysis, as this recombination reduces the number of charge carriers available for the photocatalytic reaction. A potential solution to this problem involves combining ceria with materials that have large specific surface areas and can rapidly conduct electrons, thereby reducing the recombination of photogenerated electrons and holes (e^* and h^+). Examples of such materials include reduced graphene oxide (rGO) and graphene (GP) [3–5]. The large surface area of GP and rGO provides ample active sites for the adsorption of dye molecules, thereby enhancing the efficiency of the photocatalytic process through increased catalyst–dye contact [6,7]. Furthermore, the excellent electron transport properties of graphene-based materials facilitate efficient electron transfer, lead-

ing to the generation of reactive oxygen species crucial for organic compound degradation under light irradiation [3,8].

It is noteworthy that the number of research projects on CeO_2/rGO significantly exceeds those on CeO_2/GP. Besides the fact that rGO is easier to synthesize than GP, structural differences—particularly the presence of oxygen-containing functional groups and distinct electronic properties between rGO and GP—may also account for the differences in their ability to adsorb organic dyes and the optical properties of rGO-based photocatalysts compared to GP-based photocatalysts [9,10]. The photocatalytic degradation of organic dyes is a complicated process comprising numerous stages, with the initial step involving the adsorption of dye molecules onto the surface of the photocatalyst. The photocatalytic efficiency of CeO_2/rGO and CeO_2/GP can be directly impacted by the dye adsorption capacity. The surface of rGO has demonstrated a greater affinity for adsorbing cationic dyes compared to anionic dyes [11]. In a study conducted by Mayara et al., utilizing a combination of multi-scale simulations and experiments, the authors demonstrated that the adsorption of methylene blue (MB) onto graphene oxide flakes is primarily of a physical nature and dependent on the functional groups on the surface [12]. In addition to the surface area and the presence of oxygen-containing functional groups, the existence of π-π and electrostatic interactions further enhances the adsorption capacity of rGO for cationic dyes like MB [13–15]. The adsorption capacity of MB on rGO has been documented to reach values in the range of 2000 mg/g [16], whereas the adsorption capacity of MB on GP typically amounts to approximately 200 mg/g [17], indicating the superior adsorption capacity of rGO over GP for MB.

In this study, we utilized computational chemistry methods to delve into the molecular-level reasons behind the superior photocatalytic performance of CeO_2/rGO over CeO_2/GP. Our focus was on two key aspects: (i) understanding how MB sticks to rGO and GP, shedding light on the forces driving the adsorption process; and (ii) elucidating the differences in electronic structure between CeO_2/rGO and CeO_2/GP. These findings aim to provide a clear and thorough comparison of the photocatalytic abilities of CeO_2/rGO and CeO_2/GP.

2. Results and Discussions

2.1. Adsorption Behavior of Graphene and Reduced Graphene Oxide toward Methylene Blue

A graphene model is constructed as a flat carbon layer containing 214 atoms, where the boundary carbon atoms are saturated with hydrogen atoms, corresponding to the formula $C_{214}H_{40}$ (Figure 1a). The mass fraction of carbon in this model is 98.5%, consistent with experimental analyses of the chemical composition of GP [18,19]. It should be noted that, in reality, oxygen always constitutes a small proportion of the chemical composition of GP. However, for ideal modeling purposes, we employ a completely oxygen-free GP model.

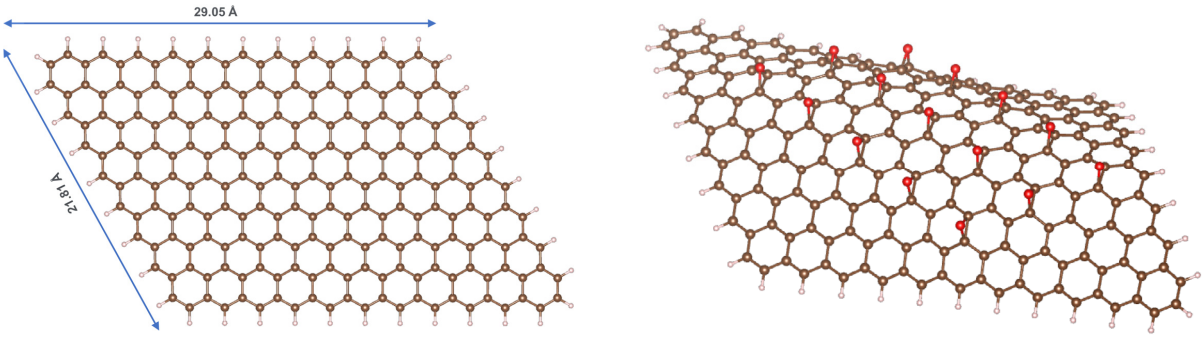

(**a**) (**b**)

Figure 1. Models of GP (**a**) and rGO (**b**); color codes: brown—C; ivory—H; red—O.

The reduced graphene oxide (rGO) model was derived from the GP model by adding the epoxide functional groups, resulting in the general formula $C_{214}H_{40}O_{15}$ (Figure 1b). The mass fractions of carbon, hydrogen, and oxygen were 90.2%, 1.40%, and 8.43%, respectively,

aligning with experimental studies [19]. Although the functional groups on the surface of rGO can be quite diverse, previous studies have demonstrated that epoxides are unique among oxygen-containing functional groups in their ability to tune the band gap. In contrast, other oxygen-containing groups are less effective: hydroxyls do not alter the band gap, and carbonyl and carboxyl groups disrupt the hexagonal carbon-ring structure of rGO [20,21].

The adsorption of MB on GP and rGO was evaluated by calculating adsorption energy values (E_{ads}) and conducting a detailed population analysis. This analysis encompassed charge transfer (q), Wiberg bond orders (BOs), molecular orbital interactions, and various other non-covalent interactions.

The adsorption energy is calculated using the following formula:

$$E_{ads} = E_{adsorbent+MB} - E_{adsorbent} - E_{MB}, \quad (1)$$

where $E_{adsorbent+MB}$ is the energy of the MB adsorption configuration on the GP or rGO adsorbent, $E_{adsorbent}$ is the energy of the adsorbent, and E_{MB} is the energy of the MB molecule.

The optimized adsorption configurations of MB on GP and rGO are shown in Figure 2, and the calculated results are presented in Table 1.

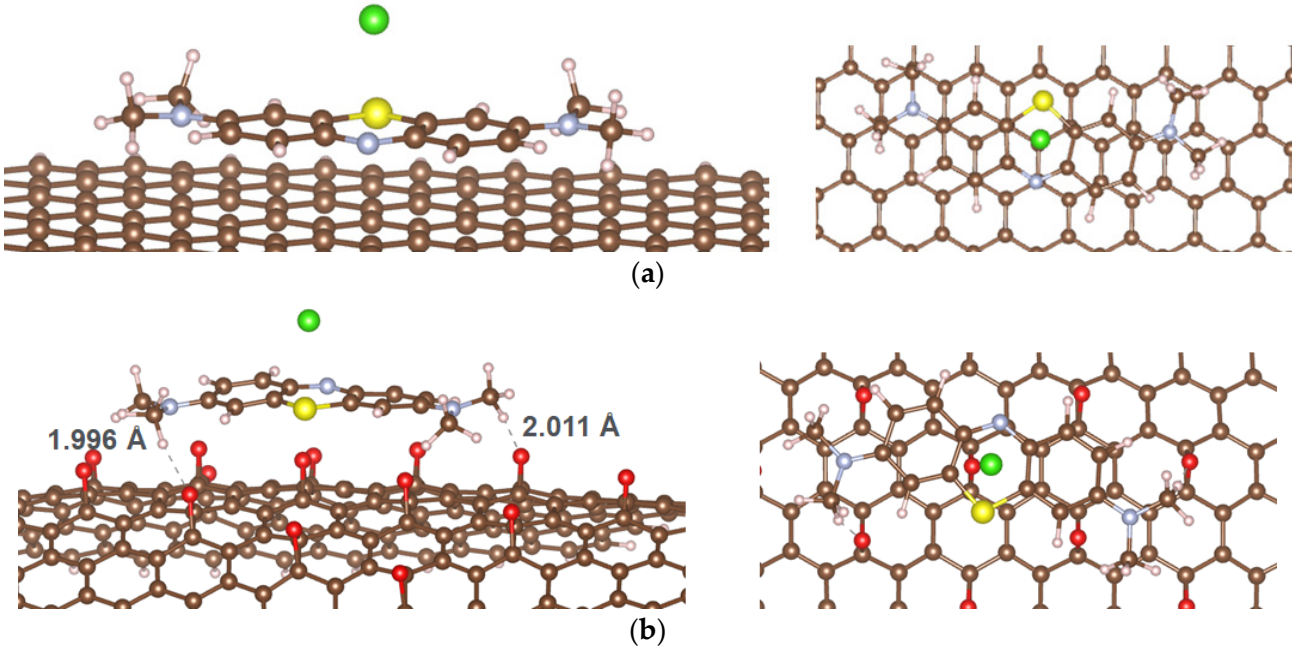

Figure 2. Optimized adsorption configurations of MB on GP (**a**) and rGO (**b**); color codes: brown—C; ivory—H, yellow—Ce; red—O; green—Cl; gray—N; light yellow—S.

Table 1. Calculated results for the adsorption of MB on GP and rGO.

Parameter	E_{ads}, kJ mol^{-1}	d_{min}, Å	q(MB), au	BO
MB/GP	−102.72	2.640 (H–C)	0.249	<0.10
MB/rGO	−405.78	1.996 (H···O)	0.411	<0.10

Note for Table 1: d_{min} is the minimal distance from the adsorbed MB molecule to the surface of the adsorbent.

The results demonstrate that the adsorption of MB on both GP and rGO is energetically favorable, as indicated by negative adsorption energy values. However, rGO exhibits a superior adsorption ability due to its significantly lower E_{ads}. The optimal adsorption configuration of MB is a parallel orientation on the adsorbent surface, consistent with previous studies [22]. This alignment is influenced by π-π stacking interactions, which are critical in the adsorption of aromatic organic compounds on carbon materials [23,24]. Despite substantial charge transfer from the MB molecule to the adsorbent, the calculations

indicate that the minimal distance from MB to the adsorbent surface and the Wiberg bond order do not suggest the formation of chemical bonds between MB and the surfaces of GP or rGO. For context, the covalent radii of carbon (C), hydrogen (H), and oxygen (O) are 0.76, 0.31, and 0.66 Å [25], respectively, while their van der Waals (vdW) radii are 1.7, 1.20, and 1.52 Å [26], respectively. Thus, the minimal distance from MB to GP or rGO is significantly larger than the sum of the covalent radii of the atoms but smaller than the sum of the vdW radii. This raises questions about the nature of the interaction force between MB and the adsorbent surfaces, given the relatively negative adsorption energy values. It is important to note that the calculated Eads differs from the experimental heat of adsorption determined from adsorption isotherms, as the calculations only consider the interaction between an MB molecule and the adsorbent surface. Due to the large size of the MB molecule and its nature as a cationic dye, the vdW and other weak interactions, as well as electrostatic interactions, are likely to play a significant role. Although the Wiberg bond order between MB and both GP and rGO is negligible, this value only accounts for covalent bonding, not other types of interactions. Therefore, we proceeded to calculate the intrinsic bond strength index (IBSI) [27] to quantify the strength of chemical bonds. The IBSI can also be used to compare the strength of weak interactions. The IBSI is expressed as

$$IBSI = \frac{(1/d^2)\int \delta g^{pair} dr}{(1/d_{H_2}^2)\int \delta g^{H_2} dr} \quad (2)$$

where d is the distance between the two atoms for which the interaction is being studied. The integral in the numerator is equivalent to the atomic pair δg index defined between the two atoms. The denominator represents the reference system data, the d_{H_2} and the integral are the bond length and atomic pair δg index of H_2 in its equilibrium structure, respectively.

The results obtained are intriguing. In the case of MB adsorption on GP, no significant IBSI value was observed between the MB atoms and the carbon atoms on the GP surface. Conversely, when adsorbed onto rGO, the hydrogen and nitrogen atoms of MB interacted with the oxygen atoms in the epoxide groups of rGO, yielding relatively high IBSI values (see Figure 3).

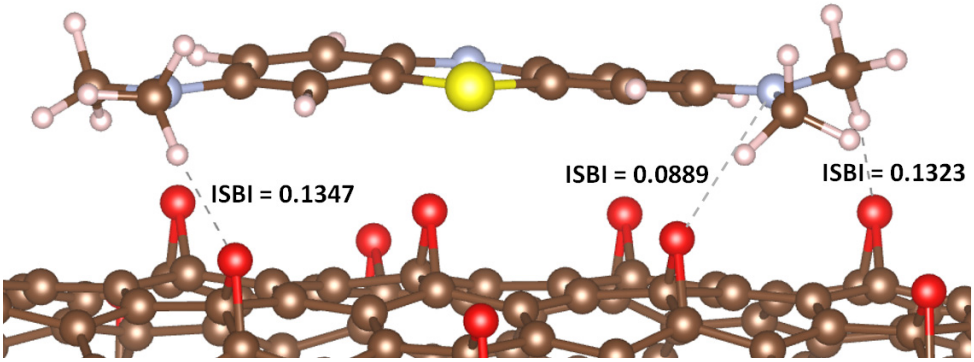

Figure 3. IBSI values corresponding to the interatomic interactions between atoms of MB and atoms of rGO.

Reduced density gradient (RDG) analysis was conducted to elucidate the weak intermolecular interactions between MB and GP, as well as between MB and rGO. The resulting map, which shows the dependence of RDG on sign (λ_2) ρ (where λ_2 is the second largest eigenvalue of the Hessian matrix of electron density and ρ is the electron density), is presented in Figure 4 for both the MB/GP and MB/rGO systems. Figure 5 depicts the RDG isosurfaces of the adsorption configurations.

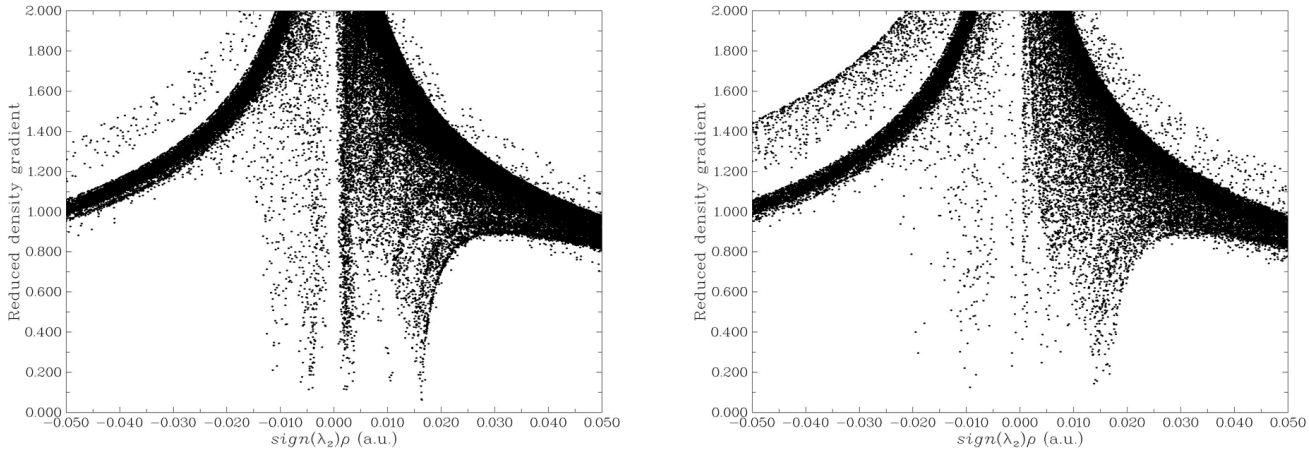

Figure 4. Scatter graph of RDG for MB/GP (**a**) and MB/rGO (**b**) systems.

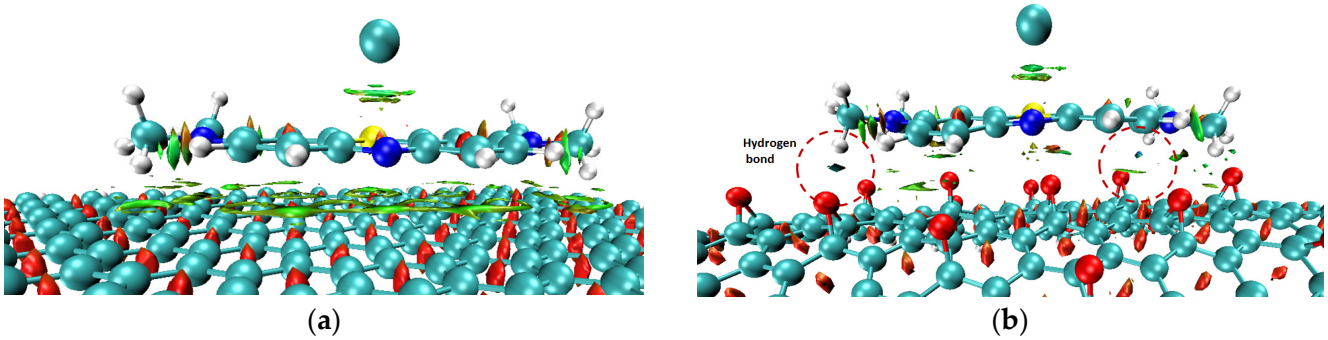

Figure 5. RDG isosurfaces (isovalue = 0.8) of MB/GP (**a**) and MB/rGO (**b**) systems.

In the case of MB/GP, the RDG graph (Figure 4a) shows spikes in the range of sign (λ_2) ρ values from −0.01 to 0.015 a.u, corresponding to vdW interactions between the MB molecule and the GP surface (colored in green in Figure 5a). Due to the flat structure of the GP surface, the vdW interactions and other weak interactions, such as π-π stacking, between MB and GP are more pronounced than on the curved surface of rGO. However, when interacting with rGO, in addition to vdW interactions similar to those with GP, there are also regions indicating hydrogen bond formation (colored in blue in Figure 5b). Additionally, the interaction between the N-H groups of MB and the oxygen atoms of rGO through hydrogen bonds or electrostatic interactions aligns well with the findings of Manash et al. [15]. Consequently, calculations of adsorption energy, along with structural parameter and population analysis, demonstrate that the adsorption of MB on rGO is more favorable than on GP.

2.2. Interaction between Graphene and Reduced Graphene Oxide with Ceria Cluster

The CeO_2-GP and CeO_2-rGO models were constructed by placing $(CeO_2)_6$ clusters on the surfaces of GP and rGO. The CeO_2 cluster model was selected to simulate small-sized CeO_2 nanoparticles dispersed on the surfaces of GP and rGO. Similar approaches using CeO_2 clusters have been employed in studies of other surface catalytic reactions [28,29].

As previously indicated, rGO demonstrates a significantly superior MB adsorption ability compared to GP due to the presence of oxygen-containing functional groups. Consequently, utilizing rGO enhances the concentration of dyes on the surface of the catalytic system, thereby creating favorable conditions for subsequent conversions at the photocatalytic centers, including ceria or rGO/MB itself. Further, we estimate the interaction of GP and rGO with ceria clusters. Effective interaction between the components in the CeO_2/GP or CeO_2/rGO catalytic system is anticipated to enhance photocatalytic activity by promoting the efficient release of photogenerated electrons and holes.

First, we calculated the interaction energy (E_{int}) between the $(CeO_2)_6$ cluster and both GP and rGO. Eint is determined using the following formula:

$$E_{int} = E_{adsorbent+cluster} - E_{adsorbent} - E_{cluster}, \quad (3)$$

where $E_{adsorbent+cluster}$ is the energy of $(CeO_2)_6$/GP or $(CeO_2)_6$/rGO, and $E_{cluster}$ is the energy of the ceria cluster.

The optimized structures of CeO_2/GP and CeO_2/rGO are shown in Figure 6. The .xyz files of these optimized structures are presented in the Supplementary Materials. Calculation results show that the interaction between $(CeO_2)_6$ and GP has an E_{int} value of +108.48 kJ mol^{-1}, while the interaction between this cluster and rGO releases 32.63 kJ mol^{-1} of energy. These findings indicate that the interaction between the ceria cluster and the GP surface is much less energetically favorable than the interaction between the cluster and rGO. The presence of oxygen-containing functional groups on the surface of rGO allows it to interact more favorably with metal-based catalysts. This result aligns well with previous experimental studies. In the work of Pandey et al. on novel three-phase polymer nanocomposites based on cerium oxide (CeO_2) nanoparticles and graphene nanoplatelets (GNPs) incorporated in poly (vinylidene fluoride) (PVDF) [30], the authors pointed out that the addition of GNPs in the PVDF/CeO_2 nanocomposites did not cause any notable change in the FTIR spectra, indicating weak or no interaction between CeO_2 and GP.

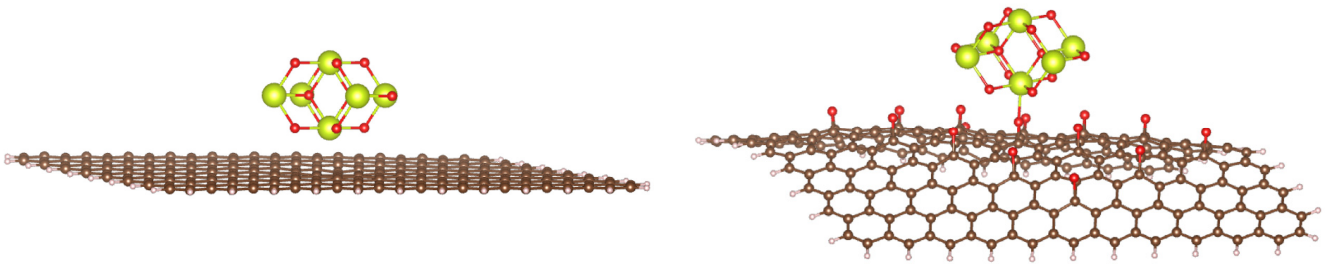

(**a**) (**b**)

Figure 6. Optimized structures of CeO_2/GP (**a**) and CeO_2/rGO (**b**).

On the other hand, the interaction between CeO_2 and rGO is energetically favorable, as evidenced by the negative E_{int} value. In fact, CeO_2/rGO material systems are widely studied in photocatalytic applications [31,32].

Due to the complexity of calculating the bandgap values for the studied materials, particularly because of the presence of an f-element (Ce), we instead evaluate the photocatalytic ability by examining the spatial distribution of HOMOs and LUMOs, as discussed in [33]. A greater spatial separation between HOMOs and LUMOs may correlate with a lower recombination rate of photogenerated electrons and holes. Figure 7 presents the frontier molecular orbitals, including the HOMO and LUMO, for the CeO_2/GP (a) and CeO_2/rGO (b) systems.

In the CeO_2/GP system, both the ceria cluster and the carbon atoms of GP mainly contribute to the HOMO and LUMO. In contrast, in the CeO_2/rGO system, the HOMO is primarily located on the ceria cluster, while the LUMO is mainly contributed by rGO. This distribution suggests that the HOMO-LUMO configuration of CeO_2/rGO will be more favorable for reducing the recombination of photogenerated electrons and holes compared to CeO_2/GP.

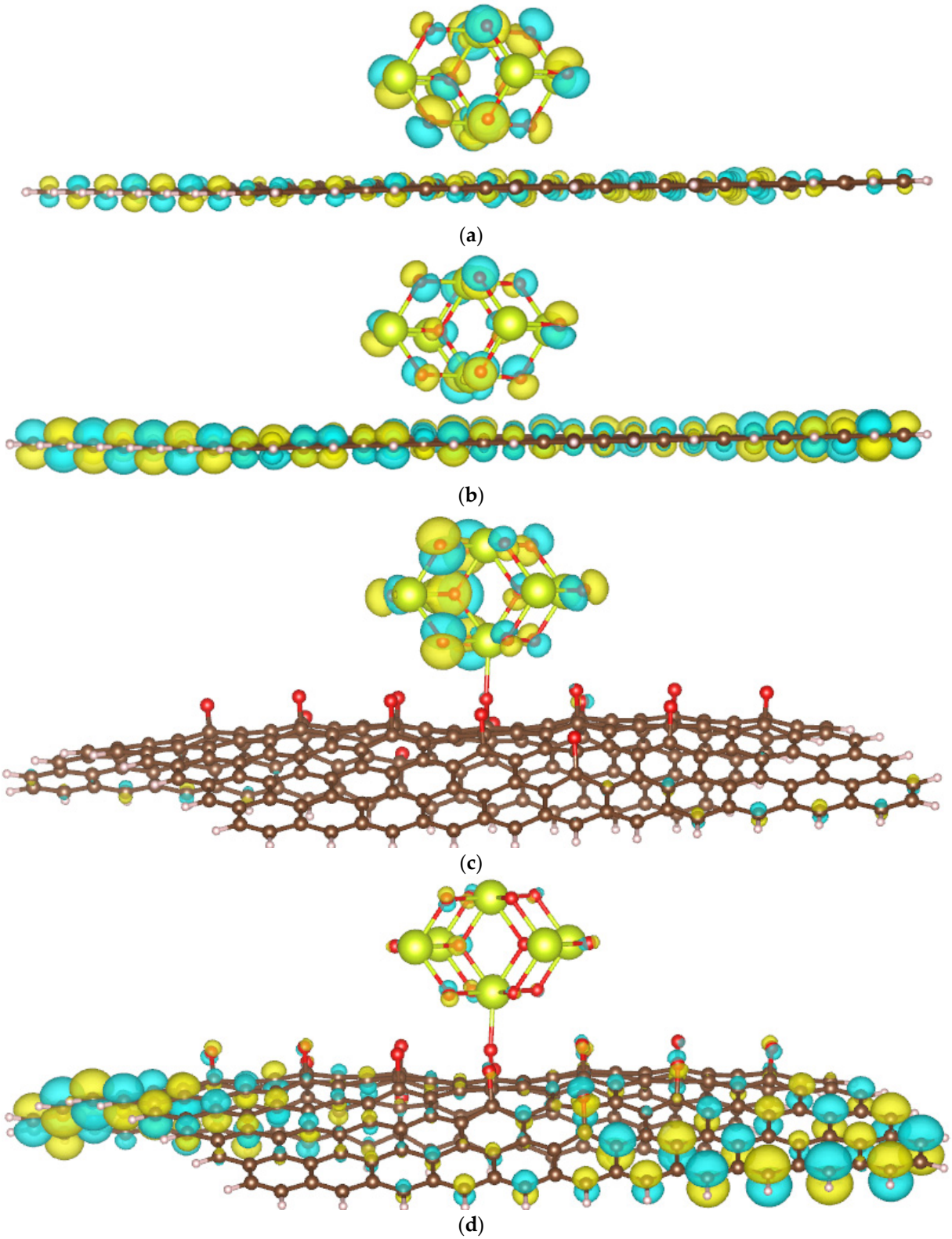

Figure 7. Frontier molecular orbitals of CeO_2/GP: HOMO (**a**) and LUMO (**b**); and CeO_2/rGO: HOMO (**c**) and LUMO (**d**).

We further calculated the fractional occupation number weighted density (FOD) to quickly and robustly provide information on the localization of "hot" (strongly correlated and chemically active) electrons in catalytic systems. The FOD map of GP and rGO (Figure 8) reveals that in the absence of CeO_2, the active electrons are concentrated on the

carbon atoms on the surface of the material. In the CeO_2/GP and CeO_2/rGO systems, active electrons are also distributed on the ceria cluster, which is particularly noticeable in the case of CeO_2/rGO. This finding is interesting when correlated with the HOMO and LUMO images of CeO_2/rGO (Figure 7c,d). The active electrons are primarily located in the HOMO of the ceria cluster, which can be excited and transferred to the LUMO located on rGO, thereby reducing the recombination ability.

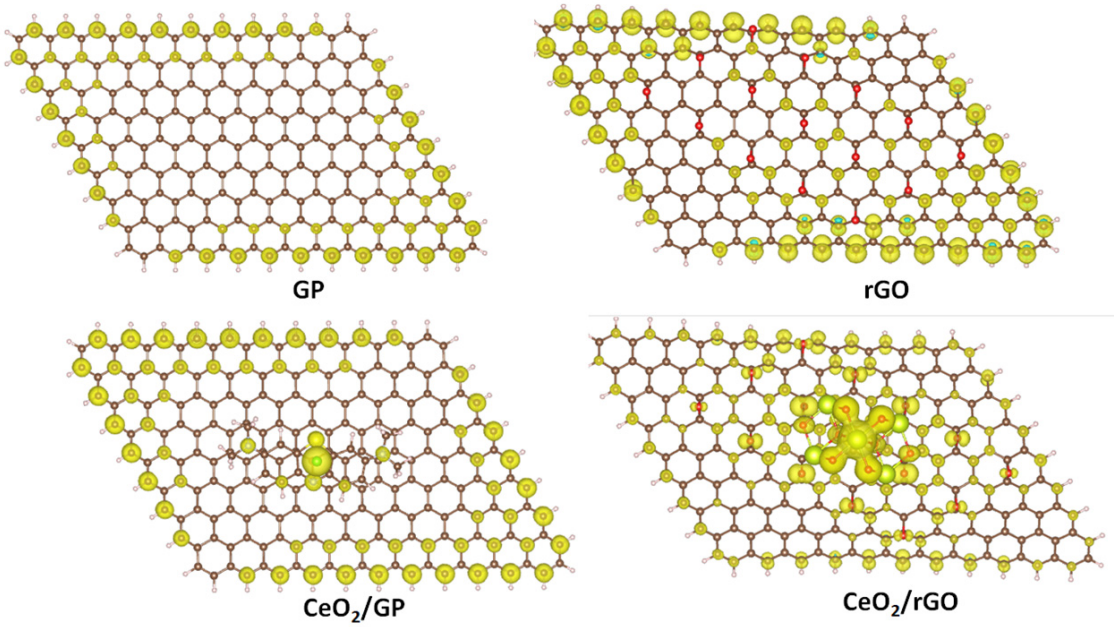

Figure 8. The FOD maps of GP, rGO, CeO_2/GP, and CeO_2/rGO.

To facilitate a more detailed analysis of charge transfer during electron excitation, we calculated the centroid distance between the HOMO and the LUMO of the photocatalytic systems. The centroid distance (D_{ij}) was determined as follows:

$$D_{ij} = \sqrt{(X_i - X_j)^2 + (Y_i - Y_j)^2 + (Z_i - Z_j)^2} \quad (4)$$

where X, Y, and Z are the coordinates of the centroid of the orbitals. The calculated results are presented in Table 2, along with parameters related to the electronic properties including absolute electronegativity (χ), the global electrophilicity index (GEI) of the photocatalytic systems, and the band gap of CeO_2/GP and CeO_2/rGO. Due to the complexities involved in calculating the UV-VIS spectra for large systems containing f-elements such as Ce, we have employed an alternative approach based on IP and EA values to evaluate the transport band gap of the studied system. According to this method, the transport band gap (E_g) is defined as E_g = IP − EA [34,35].

Table 2. Electronic properties and E_g of $(CeO_2)_6$, GP, rGO CeO_2/GP, and CeO_2/rGO.

System	D_{ij}, Å	χ, eV	GEI, eV	E_g, eV
$(CeO_2)_6$	0.023	5.3792	3.4417	-
GP	0.029	5.0983	8.7913	-
rGO	8.181	5.4622	10.0683	-
CeO_2/GP	3.472	8.7657	26.6079	1.4439
CeO_2/rGO	9.666	7.6218	20.7440	1.4001

The computational results indicate that the calculated E_g values of CeO_2/GP and CeO_2/rGO are relatively close to each other and smaller than the experimental values. It is important to note that, due to the size limitations of the model, the calculated band gap

values for the studied systems are intended to assess the trends in variation rather than provide absolute values. Experimental measurements reveal that the optical band gap values of CeO_2/GP and CeO_2/rGO are also relatively similar, approximately 2.7 eV [31,36]. Therefore, from the standpoint of light absorption capability, there is no significant difference between CeO_2/GP and CeO_2/rGO. Consequently, the variation in photocatalytic activity is likely primarily attributed to the recombination rates of photogenerated electrons and holes.

The *Dij* value of the material systems increases in the following order: $(CeO_2)_6$ < GP < CeO_2/GP < rGO < CeO_2/rGO. This indicates that combining ceria with GP and rGO can significantly reduce the recombination ability of photogenerated electrons and holes. Among the studied material systems, the CeO_2/rGO system exhibits the best ability to separate e^*–h^+.

The incorporation of ceria into GP and rGO increases both the absolute electronegativity value and the global electrophilicity index (GEI) compared to the original materials. Notably, the GEI can be used as a measure of Lewis acidity [37,38]. Previous studies have highlighted a positive correlation between Lewis acidity, or the number of Lewis acid centers, and the photocatalytic decomposition activity of methylene blue and rhodamine B in photocatalysts [39,40]. Therefore, the increased GEI value of material systems due to the presence of ceria is favorable for the decomposition of methylene blue.

3. Computational Methods

All geometry calculations were performed using density functional theory (DFT) methods, as implemented in the CP2K code (https://www.cp2k.org/). The exchange-correlation potential was described using the generalized gradient approximation (GGA) with the Perdew–Burke–Ernzerhof (PBE) spin-polarized functional [41]. Wavefunctions were expanded using a double-zeta valence polarized (DZVP) basis set, supplemented by an auxiliary plane-wave basis with a cutoff energy of 250 Ry. Core electrons were modeled using norm-conserving pseudopotentials [42]. Brillouin zone integration was performed using a reciprocal space mesh that included only the Γ-point. Dudarev's approach for DFT+U calculations was employed to describe the Ce 4f electrons [43]. It should be noted that the bandgap value of the bulk CeO_2 varies from 2.94 to 3.42 eV [44]. However, this value varies significantly for the $(CeO_2)_6$ cluster model due to the influence of cluster structures and sizes. In this study, a U–J value of 16.0 eV was used, corresponding to the highest bandgap value simulated for the $(CeO_2)_6$ cluster, which is 1.99 eV. Additionally, van der Waals forces were included using DFT-D calculations based on the Grimme D3 method to accurately estimate interaction forces [45].

The electronic properties of the studied systems, specifically the vertical ionization energy (IP), vertical electron affinity (EA), and global electrophilicity index (GEI), were determined through single-point calculations utilizing the GFN1-xTB method [46,47]. Non-covalent interactions were analyzed using Multiwfn software v3.8 [48].

4. Conclusions

The superior photocatalytic efficacy of CeO_2/rGO over CeO_2/GP in the photodegradation of methylene blue has been demonstrated through the evaluation of MB adsorption on the rGO substrate relative to GP, alongside an examination of the electronic characteristics inherent to these catalytic systems. The calculated adsorption energy and population analysis reveal that the adsorption of MB onto both GP and rGO is energetically favorable, primarily driven by non-covalent interactions, including van der Waals forces, π-π stacking interactions, and electrostatic interactions. Notably, rGO exhibits a heightened MB adsorption capacity relative to GP, attributable to the formation of weak bonds such as hydrogen bonds with oxygen atoms on its surface. The calculated interaction energies indicate that the combination of ceria with GP lacks energetic favorability compared to rGO. Through a comprehensive assessment of frontier molecular orbitals, fractional occupation density, the centroid distance between molecular orbitals, and the Lewis acid index of the catalysts,

it has been demonstrated that CeO_2/rGO exhibits superior efficacy in the separation of photogenerated electrons and holes compared to CeO_2/GP. These findings hold substantial implications for understanding the mechanisms governing the photocatalytic degradation of organic dyes, as well as for the development of novel effective photocatalysts.

Supplementary Materials: The following supporting information can be downloaded at: https://www.mdpi.com/article/10.3390/molecules29163821/s1. Coordinates of atoms for the optimized CeO_2/rGO and CeO_2/GP structures.

Author Contributions: Conceptualization, N.T.T.H.; Methodology, L.M.C. and N.T.T.H.; Formal analysis, N.H.H., N.N.H. and L.M.C.; Investigation, N.H.H., P.T.L., N.N.H. and L.M.C.; Data curation, P.T.L.; Writing—original draft, N.H.H. and N.T.T.H.; Writing—review & editing, N.T.T.H.; Funding acquisition, N.H.H. All authors have read and agreed to the published version of the manuscript.

Funding: This work is funded by the Ministry of Education and Training under grant no. B2022-TDV-06.

Institutional Review Board Statement: Not applicable.

Informed Consent Statement: Not applicable.

Data Availability Statement: The data that support the findings of this study are available from the corresponding author upon reasonable request.

Conflicts of Interest: The authors declare that they have no conflicts of interest.

References

1. Tkaczyk, A.; Mitrowska, K.; Posyniak, A. Synthetic organic dyes as contaminants of the aquatic environment and their implications for ecosystems: A review. *Sci. Total Environ.* **2020**, *717*, 137222. [CrossRef] [PubMed]
2. Reddy, P.A.K.; Reddy, P.V.L.; Kwon, E.; Kim, K.-H.; Akter, T.; Kalagara, S. Recent advances in photocatalytic treatment of pollutants in aqueous media. *Environ. Int.* **2016**, *91*, 94–103. [CrossRef] [PubMed]
3. Khan, M.A.M.; Rani, S.; Ansari, A.A.; Ahamed, M.; Ahmed, J.; Kumar, S.; Rana, A.U.H.S. Anchoring Ceria Nanoparticles on Reduced Graphene Oxide and Their Enhanced Photocatalytic and Electrochemical Activity for Environmental Remediation. *J. Electron. Mater.* **2023**, *53*, 930–944. [CrossRef]
4. Barik, M.; Das, D.; Satapathy, P.K.; Mohapatra, P. Graphene supported ceria-titania mixed oxide composite-An effective photo catalyst for methylene blue (MB) dye degradation. *Environ. Eng. Res.* **2023**, *28*, 220586. [CrossRef]
5. Singh, R.; Kumar, M.; Khajuria, H.; Tashi, L.; Sheikh, H.N. Nitrogen-doped graphene-cerium oxide (NG-CeO_2) photocatalyst for the photodegradation of methylene blue in waste water. *J. Chin. Chem. Soc.* **2018**, *66*, 467–473. [CrossRef]
6. Shabil Sha, M.; Anwar, H.; Musthafa, F.N.; Al-Lohedan, H.; Alfarwati, S.; Rajabathar, J.R.; Khalid Alahmad, J.; Cabibihan, J.-J.; Karnan, M.; Kumar Sadasivuni, K. Photocatalytic degradation of organic dyes using reduced graphene oxide (rGO). *Sci. Rep.* **2024**, *14*, 3608. [CrossRef] [PubMed]
7. Kamedulski, P.; Skorupska, M.; Binkowski, P.; Arendarska, W.; Ilnicka, A.; Lukaszewicz, J.P. High surface area micro-mesoporous graphene for electrochemical applications. *Sci. Rep.* **2021**, *11*, 22054. [CrossRef] [PubMed]
8. Das, D.; Das, M.; Sil, S.; Sahu, P.; Ray, P.P. Effect of Higher Carrier Mobility of the Reduced Graphene Oxide–Zinc Telluride Nanocomposite on Efficient Charge Transfer Facility and the Photodecomposition of Rhodamine B. *ACS Omega* **2022**, *7*, 26483–26494. [CrossRef]
9. Yang, H.; Hu, H.; Ni, Z.; Poh, C.K.; Cong, C.; Lin, J.; Yu, T. Comparison of surface-enhanced Raman scattering on graphene oxide, reduced graphene oxide and graphene surfaces. *Carbon* **2013**, *62*, 422–429. [CrossRef]
10. Hidayah, N.M.S.; Liu, W.-W.; Lai, C.-W.; Noriman, N.Z.; Khe, C.-S.; Hashim, U.; Lee, H.C. Comparison on graphite, graphene oxide and reduced graphene oxide: Synthesis and characterization. *AIP Conf. Proc.* **2017**, *1892*, 150002. [CrossRef]
11. Kim, H.; Kang, S.-O.; Park, S.; Park, H.S. Adsorption isotherms and kinetics of cationic and anionic dyes on three-dimensional reduced graphene oxide macrostructure. *J. Ind. Eng. Chem.* **2015**, *21*, 1191–1196. [CrossRef]
12. Leão, M.B.; Vendrame, L.F.O.; Fagan, S.B.; Zanella, I.; Jauris, I.M.; Bordin, J.R.; De Matos, C.F. Combining multi-scale simulations and experiments to unveil the adsorption of methylene blue in graphene tridimensional-based materials. *Mol. Syst. Des. Eng.* **2023**, *8*, 666–680. [CrossRef]
13. Xiao, J.; Lv, W.; Xie, Z.; Tan, Y.; Song, Y.; Zheng, Q. Environmentally friendly reduced graphene oxide as a broad-spectrum adsorbent for anionic and cationic dyes via π–π interactions. *J. Mater. Chem. A* **2016**, *4*, 12126–12135. [CrossRef]
14. Minitha, C.R.; Lalitha, M.; Jeyachandran, Y.L.; Senthilkumar, L.; Rt, R.K. Adsorption behaviour of reduced graphene oxide towards cationic and anionic dyes: Co-action of electrostatic and π–π interactions. *Mater. Chem. Phys.* **2017**, *194*, 243–252. [CrossRef]

15. Sharma, P.; Hussain, N.; Borah, D.J.; Das, M.R. Kinetics and Adsorption Behavior of the Methyl Blue at the Graphene Oxide/Reduced Graphene Oxide Nanosheet–Water Interface: A Comparative Study. *J. Chem. Eng. Data* **2013**, *58*, 3477–3488. [CrossRef]
16. Jahan, N.; Roy, H.; Reaz, A.H.; Arshi, S.; Rahman, E.; Firoz, S.H.; Islam, M.S. A comparative study on sorption behavior of graphene oxide and reduced graphene oxide towards methylene blue. *Case Stud. Chem. Environ. Eng.* **2022**, *6*, 100239. [CrossRef]
17. Liu, T.; Li, Y.; Du, Q.; Sun, J.; Jiao, Y.; Yang, G.; Wang, Z.; Xia, Y.; Zhang, W.; Wang, K.; et al. Adsorption of methylene blue from aqueous solution by graphene. *Colloids Surf. B Biointerfaces* **2012**, *90*, 197–203. [CrossRef] [PubMed]
18. Zhu, B.; Qu, C.; Gao, S.; Liang, Z.; Zhang, H.; Zou, R. Ultralow Loading Ruthenium Nanoparticles on Nitrogen-Doped Graphene Aerogel for Trifunctional Electrocatalysis. *ChemCatChem* **2018**, *10*, 1113–1121. [CrossRef]
19. Albers, P.W.; Leich, V.; Ramirez-Cuesta, A.J.; Cheng, Y.; Hönig, J.; Parker, S.F. The characterisation of commercial 2D carbons: Graphene, graphene oxide and reduced graphene oxide. *Mater. Adv.* **2022**, *3*, 2810–2826. [CrossRef]
20. Jin, Y.; Zheng, Y.; Podkolzin, S.G.; Lee, W. Band gap of reduced graphene oxide tuned by controlling functional groups. *J. Mater. Chem. C* **2020**, *8*, 4885–4894. [CrossRef]
21. Van Khai, T.; Viet Hai, L.; Thi Thu Ha, N.; Thi Thom, N.; Van Trang, N.; Thi Nam, P.; Ngoc Ha, N.; Dai Lam, T. Combined experimental and theoretical studies on enlarged bandgap and improved photoelectrochemical properties of reduced graphene oxide film by hydrogen annealing. *J. Electroanal. Chem.* **2021**, *900*, 115722. [CrossRef]
22. Liu, H.; An, Q.; Deng, Q.; Ming, J.; Xu, H. Adsorption behavior of methylene blue on graphene and hexagonal boron nitride monolayers in aqueous solution: A first-principles treatment. *J. Phys. Chem. Solids* **2023**, *174*, 111151. [CrossRef]
23. Björk, J.; Hanke, F.; Palma, C.-A.; Samori, P.; Cecchini, M.; Persson, M. Adsorption of Aromatic and Anti-Aromatic Systems on Graphene through $\pi-\pi$ Stacking. *J. Phys. Chem. Lett.* **2010**, *1*, 3407–3412. [CrossRef]
24. Cao, M.; Fu, A.; Wang, Z.; Liu, J.; Kong, N.; Zong, X.; Liu, H.; Gooding, J.J. Electrochemical and Theoretical Study of π–π Stacking Interactions between Graphitic Surfaces and Pyrene Derivatives. *J. Phys. Chem. C* **2014**, *118*, 2650–2659. [CrossRef]
25. Cordero, B.; Gómez, V.; Platero-Prats, A.E.; Revés, M.; Echeverría, J.; Cremades, E.; Barragán, F.; Alvarez, S. Covalent radii revisited. *Dalton Trans.* **2008**, *21*, 2832. [CrossRef] [PubMed]
26. Bondi, A. van der Waals Volumes and Radii. *J. Phys. Chem.* **1964**, *68*, 441–451. [CrossRef]
27. Klein, J.; Khartabil, H.; Boisson, J.-C.; Contreras-García, J.; Piquemal, J.-P.; Hénon, E. New Way for Probing Bond Strength. *J. Phys. Chem. A* **2020**, *124*, 1850–1860. [CrossRef] [PubMed]
28. Jiang, Y.; Mao, K.; Li, J.; Duan, D.; Li, J.; Wang, X.; Zhong, Y.; Zhang, C.; Liu, H.; Gong, W.; et al. Pushing the Performance Limit of Cu/CeO_2 Catalyst in CO2 Electroreduction: A Cluster Model Study for Loading Single Atoms. *ACS Nano* **2023**, *17*, 2620–2628. [CrossRef]
29. Bjerregaard, J.D.; Mikkelsen, K.V.; Johnson, M.S. Hybrid DFT small-cluster model of CO oxidation on CeO_2/(110). *Chem. Phys. Lett.* **2022**, *793*, 139436. [CrossRef]
30. Pandey, M.; Deshmukh, K.; Dhandapani, K.; Singh, R.S. Influence of Nano-CeO_2 and Graphene Nanoplatelets on the Conductivity and Dielectric Properties of Poly(vinylidene fluoride) Nanocomposite Films. *Langmuir* **2024**, *40*, 1909–1921. [CrossRef]
31. Balsamo, S.A.; La Greca, E.; Calà Pizzapilo, M.; Sciré, S.; Fiorenza, R. CeO_2-rGO Composites for Photocatalytic H_2 Evolution by Glycerol Photoreforming. *Materials* **2023**, *16*, 747. [CrossRef] [PubMed]
32. Sagadevan, S.; Johan, M.R.; Lett, J.A. Fabrication of reduced graphene oxide/CeO_2 nanocomposite for enhanced electrochemical performance. *Appl. Phys. A* **2019**, *125*, 315. [CrossRef]
33. Ha, N.T.T.; Be, P.T.; Lan, P.T.; Mo, N.T.; Cam, L.M.; Ha, N.N. Whether planar or corrugated graphitic carbon nitride combined with titanium dioxide exhibits better photocatalytic performance? *RSC Adv.* **2021**, *11*, 16351–16358. [CrossRef] [PubMed]
34. Louis, E.; San-Fabián, E.; Díaz-García, M.A.; Chiappe, G.; Vergés, J.A. Are Electron Affinity and Ionization Potential Intrinsic Parameters to Predict the Electron or Hole Acceptor Character of Amorphous Molecular Materials? *J. Phys. Chem. Lett.* **2017**, *8*, 2445–2449. [CrossRef] [PubMed]
35. Bredas, J.L. Mind the gap! *Mater. Horiz.* **2014**, *1*, 17–19. [CrossRef]
36. Khan, M.E.; Khan, M.M.; Cho, M.H. Ce^{3+}-ion, Surface Oxygen Vacancy, and Visible Light-induced Photocatalytic Dye Degradation and Photocapacitive Performance of CeO_2-Graphene Nanostructures. *Sci. Rep.* **2017**, *7*, 5928. [CrossRef] [PubMed]
37. Jupp, A.R.; Johnstone, T.C.; Stephan, D.W. The global electrophilicity index as a metric for Lewis acidity. *Dalton Trans.* **2018**, *47*, 7029–7035. [CrossRef] [PubMed]
38. Jupp, A.R.; Johnstone, T.C.; Stephan, D.W. Improving the Global Electrophilicity Index (GEI) as a Measure of Lewis Acidity. *Inorg. Chem.* **2018**, *57*, 14764–14771. [CrossRef] [PubMed]
39. Hassan, S.M.; Ahmed, A.I.; Mannaa, M.A. Surface acidity, catalytic and photocatalytic activities of new type H3PW12O40/Sn-TiO_2 nanoparticles. *Colloids Surf. A Physicochem. Eng. Asp.* **2019**, *577*, 147–157. [CrossRef]
40. Cui, H.; Dwight, K.; Soled, S.; Wold, A. Surface Acidity and Photocatalytic Activity of Nb_2O_5/TiO_2 Photocatalysts. *J. Solid State Chem.* **1995**, *115*, 187–191. [CrossRef]
41. Perdew, J.P.; Burke, K.; Ernzerhof, M. Generalized Gradient Approximation Made Simple. *Phys. Rev. Lett.* **1996**, *77*, 3865–3868. [CrossRef] [PubMed]
42. Hamann, D.R.; Schlüter, M.; Chiang, C. Norm-Conserving Pseudopotentials. *Phys. Rev. Lett.* **1979**, *43*, 1494–1497. [CrossRef]
43. Dudarev, S.L.; Botton, G.A.; Savrasov, S.Y.; Humphreys, C.J.; Sutton, A.P. Electron-energy-loss spectra and the structural stability of nickel oxide: An LSDA+U study. *Phys. Rev. B* **1998**, *57*, 1505–1509. [CrossRef]

44. Huang, Y.-C.; Wu, S.-H.; Hsiao, C.-H.; Lee, A.-T.; Huang, M.H. Mild Synthesis of Size-Tunable CeO_2 Octahedra for Band Gap Variation. *Chem. Mater.* **2020**, *32*, 2631–2638. [CrossRef]
45. Grimme, S.; Antony, J.; Ehrlich, S.; Krieg, H. A consistent and accurateab initioparametrization of density functional dispersion correction (DFT-D) for the 94 elements H-Pu. *J. Chem. Phys.* **2010**, *132*, 154104–154119. [CrossRef] [PubMed]
46. Bannwarth, C.; Ehlert, S.; Grimme, S. GFN2-xTB—An Accurate and Broadly Parametrized Self-Consistent Tight-Binding Quantum Chemical Method with Multipole Electrostatics and Density-Dependent Dispersion Contributions. *J. Chem. Theory Comput.* **2019**, *15*, 1652–1671. [CrossRef] [PubMed]
47. Grimme, S.; Bannwarth, C.; Shushkov, P. A Robust and Accurate Tight-Binding Quantum Chemical Method for Structures, Vibrational Frequencies, and Noncovalent Interactions of Large Molecular Systems Parametrized for All spd-Block Elements (Z = 1–86). *J. Chem. Theory Comput.* **2017**, *13*, 1989–2009. [CrossRef]
48. Lu, T.; Chen, F. Multiwfn: A multifunctional wavefunction analyzer. *J. Comput. Chem.* **2011**, *33*, 580–592. [CrossRef]